NAVAL POSTGRADUATE SCHOOL
MONTEREY, CALIFORNIA

THESIS

SODIUM SULFATE HOT CORROSION OF SILICON CARBIDE FIBER-REINFORCED CALCIUM ALUMINOSILICATE
by

Maria A. Oppici

March 1995

Thesis Advisor: **Alan G. Fox**
Thesis Co-Advisor: **Atul Kumar**

Approved for public release; distribution is unlimited.

REPORT DOCUMENTATION PAGE

Form Approved OMB No. 0704-0188

1. AGENCY USE ONLY *(Leave blank)*	2. REPORT DATE March 1995	3. REPORT TYPE AND DATES COVERED Master's Thesis

4. TITLE AND SUBTITLE SODIUM SULFATE HOT CORROSION OF SILICON CARBIDE FIBER-REINFORCED CALCIUM ALUMINOSILICATE

5. FUNDING NUMBERS

6. AUTHOR(S) Oppici, Maria A.

7. PERFORMING ORGANIZATION NAME(S) AND ADDRESS(ES)
Naval Postgraduate School
Monterey CA 93943-5000

8. PERFORMING ORGANIZATION REPORT NUMBER

9. SPONSORING/MONITORING AGENCY NAME(S) AND ADDRESS(ES)
Naval Air Warefare Center
Warminster, PA 18974

10. SPONSORING/MONITORING AGENCY REPORT NUMBER

11. SUPPLEMENTARY NOTES The views expressed in this thesis are those of the author and do not reflect the official policy or position of the Department of Defense or the U.S. Government.

12a. DISTRIBUTION/AVAILABILITY STATEMENT
Approved for public release; distribution is unlimited.

12b. DISTRIBUTION CODE

13. ABSTRACT *(maximum 200 words)*
*

The effects of sodium sulfate hot corrosion on the microstructure of silicon carbide fiber-reinforced calcium aluminosilicate glass-ceramic matrix composite were investigated using optical microscopy, scanning electron microscopy (SEM) and x-ray diffraction (XRD). Hot corrosion of samples at 900°C for 50 hours in both air and argon was investigated. SEM and XRD investigations of the sample exposed in air revealed a complex mixture of wollastonite, nepheline and albite whereas exposure in argon showed pseudowollastonite, nepheline and calcium sulfide. It was observed that the presence of Na_2SO_4 enhanced the oxidation of the silicon carbide fiber to silica which further reacted to form the products of corrosion.

14. SUBJECT TERMS			15. NUMBER OF PAGES 68
			16. PRICE CODE
17. SECURITY CLASSIFICATION OF REPORT Unclassified	18. SECURITY CLASSIFICATION OF THIS PAGE Unclassified	19. SECURITY CLASSIFICATION OF ABSTRACT Unclassified	20. LIMITATION OF ABSTRACT UL

NSN 7540-01-280-5500 Standard Form 298 (Rev. 289) Prescribed by ANSI Std. 239-18 298-102

Approved for public release; distribution is unlimited.

SODIUM SULFATE HOT CORROSION OF SILICON CARBIDE FIBER-REINFORCED CALCIUM ALUMINOSILICATE

Maria A. Oppici
Lieutenant, United States Navy
B.A., Columbia University, 1983

Submitted in partial fulfillment
of the requirements for the degree of

MASTER OF SCIENCE IN MECHANICAL ENGINEERING
from the
NAVAL POSTGRADUATE SCHOOL
March 1995

Author: _____
Maria A. Oppici

Approved by: _____
Alan G. Fox, Thesis Advisor

_____
Atul Kumar, Thesis Co-advisor

_____
Matthew D. Kelleher, Chairman
Department of Mechanical Engineering

ABSTRACT

The effects of sodium sulfate hot corrosion on the microstructure of silicon carbide fiber-reinforced calcium aluminosilicate glass-ceramic matrix composite were investigated using optical microscopy, scanning electron microscopy (SEM) and x-ray diffraction (XRD). Hot corrosion of samples at 900°C for 50 hours in both air and argon was investigated. SEM and XRD investigations of the sample exposed in air revealed a complex mixture of wollastonite, nepheline and albite whereas exposure in argon showed pseudowollastonite, nepheline and calcium sulfide. It was observed that the presence of Na_2SO_4 enhanced the oxidation of the silicon carbide fiber to silica which further reacted to form the products of corrosion.

TABLE OF CONTENTS

I. INTRODUCTION 1

II. BACKGROUND 3

A. THE CALCIUM ALUMINOSILICATE SYSTEM (CAS) 3

B. SILICON CARBIDE (SiC) FIBER-REINFORCED CAS COMPOSITES 5

C. CORROSION OF SiC/CAS COMPOSITES BY Na_2SO_4 8

III. SCOPE OF PRESENT WORK 13

IV. EXPERIMENTAL PROCEDURE 15

A. OPTICAL MICROSCOPY 17

B. X-RAY DIFFRACTION (XRD) 17

C. SCANNING ELECTRON MICROSCOPE (SEM) 18

V. RESULTS AND DISCUSSION 21

A. XRD ANALYSIS 21

B. OPTICAL AND SCANNING ELECTRON MICROSCOPY ANALYSIS 31

C. DISCUSSION 44

VI. CONCLUSIONS 47

VII. RECOMMENDATIONS 49

LIST OF REFERENCES 51

INITIAL DISTRIBUTION LIST 53

LIST OF TABLES

I. CAS, SiC, and SiC/CAS Material Properties 5

II. Matrix Composition 17

III. Summary of XRD Results 21

IV. As-prepared SiC/CAS EDX Results and Expected Compositions 32

V. Elemental Weight Percentages for Expected Products 37

VI. EDX Weight Percent Analysis of Na_2SO_4 Coated Sample Heat treated in Air 37

VII. EDX Weight Percent Analysis of Na_2SO_4 Coated Sample Heat treated in Argon ... 42

LIST OF FIGURES

1. CAS Phase Diagram 4
2. Fracture Mechanism Map for a Uniaxial Fiber 6
3. Stress/Strain Curve for $[0°]_8$ SiC/CAS 7
4. Dewpoints For Na_2SO_4 Deposition 9
5. Hot Corrosion Region as a Function of Reciprocal Temperature 10
6. Stress Strain Curves of SiC/CAS Tensile Specimens 11
7. SiC/CAS Fabrication Process Schematic 15
8. XRD Pattern of As-prepared SiC/CAS Sample 23
9. XRD Line Patterns of Phases Present in As-prepared SiC/CAS 24
10. Comparison of XRD Patterns of (a) As-prepared, (b) Salt Coated and heat treated in air and (c) Salt Coated and Heat treated in Argon 25
11. XRD Pattern of SiC/CAS Sample Heat Treated in Air Showing Crystalline Phases 27
12. XRD Line Patterns of Phases Present in SiC/CAS Heat Treated in Air 28
13. XRD Pattern of SiC/CAS Sample Heat Treated in Argon Showing Crystalline Phases 29
14. XRD Line Patterns of Phases Present in SiC/CAS Heat Treated in Argon 30
15. System $CaO{\cdot}SiO_2$-$Na_2O{\cdot}Al_2O_3{\cdot}2SiO_2$ Phase Diagram 31

16. Optical Micrograph of the As-prepared Sample 31

17. BSE SEM Micrograph and EDX Maps of the As-prepared Sample..... 33

18. Optical Micrograph of the Sample Heat Treated in Air 34

19. BSE SEM Image of the Sample Heat Treated in Air 36

20. BSE SEM Micrograph and EDX Maps of the Sample Heat Treated in Air..... 36

21. (a) BSE SEM Image and (b) EDX Line Analysis of Partially Corroded Fiber in the Sample Heat Treated in Air..... 38

22. Optical Micrograph of the Sample Heat Treated in Argon..... 39

23. BSE SEM Micrograph and EDX Maps of the Sample Heat Treated in Argon..... 41

24. Secondary Electron SEM Micrograph of the Surface of the Sample Heat Treated in Argon - Unpolished 42

25. Secondary Electron SEM Micrograph of the Sample Heat Treated in Argon Showing the Polished Surface 43

26. Secondary Electron SEM Micrograph of the Sample Heat Treated in Argon Polished to Show a Corroded Fiber..... 43

ACKNOWLEDGMENTS

I would like to extend my sincere appreciation to Professor Alan G. Fox and Doctor Atul Kumar, my thesis advisors, for their expertise and guidance in the preparation of this thesis. They made this a worthwhile and enlightening process for all of their patience and dedication to this field of study.

I. INTRODUCTION

Ceramic matrix composites are potential candidates for high temperature structural components due to their low density and improved toughness compared to monolithic ceramics. This has led the U. S. Navy to investigate their use in gas turbine engines. Presently, nickel-based superalloys are being used for gas turbine engine components and the motivation for replacement of these by ceramic matrix composites is improved engine performance.

Current gas turbine design is restricted by the properties of the metal superalloys. Their high density limits maximum turbine speed, due to increased stresses incurred at high rotation speeds and increased weight, which is critical in aircraft, and decreases performance by reducing thrust to weight ratio. The maximum operating temperature of the superalloys is also below that required to optimize engine efficiency by combustion of fuel at stoichiometric ratios which increases temperatures dramatically, especially at the inlet to the power turbine.

These temperature restrictions could be overcome by utilizing monolithic ceramics since they are lighter than the superalloys, can withstand the extreme temperatures required and offer the added advantage of low coefficients of thermal expansion which reduce engine stresses. Unfortunately, monolithic ceramics are extremely brittle and could not withstand the mechanical stresses of the turbine engine. However, increased toughness can be achieved by reinforcement of the ceramic with fibers.

One such system is silicon carbide fiber-reinforced calcium aluminosilicate (SiC/CAS) glass-ceramic matrix composite (CMC) which has been shown to exhibit high temperature oxidation resistance with only a modest decrease in mechanical properties [Ref. 6,10].

The effects of the marine operating environment on this CMC have yet to be established. It has been shown that, in this environment, the mixture of salt and impurity sulfur in the fuel can lead to deposition of sodium sulfate (Na_2SO_4) salt on engine parts. This, in conjunction with the high temperatures, can lead to corrosion of the CMC which is often termed hot corrosion.

Hot corrosion of many monolithic ceramics by Na_2SO_4 has been well documented but there is evidence that hot corrosion of glass ceramic matrix composite systems is more complex and this needs to be properly understood before the possible use of CMCs for Naval applications.

II. BACKGROUND

A. THE CALCIUM ALUMINOSILICATE SYSTEM (CAS)

Calcium aluminosilicate glass ceramic is a crystalline material formed by controlled crystallization of a glassy mixture by heat treatment with nucleating agents to produce a fine-grained uniform crystalline ceramic microstructure which also contains some residual glassy phases. The advantage of this system is that it allows processing at relatively low temperatures, (a glass property), while the crystalline phases allow use at higher temperatures than glass, although not quite as high as conventional ceramics. Also, customization of the glass-ceramic thermal expansion can be achieved by varying heat treatments. In addition, the fine grained microstructure greatly improves the strength of the material.

The drawback to this system is that it is limited by brittleness i.e. low strain to failure, low tensile strength and low fracture toughness. This brittle behavior has been explained by the pile up of dislocations due to the dearth of slip planes, which dislocations could move along, and strong ionic bonds which would have to be broken for dislocation motion. Because of this, crack propagation cannot be blunted by plastic deformation and crack initiation leads to failure at relatively low strains.

The phase diagram of the calcium aluminosilicate system is shown in Figure 1. [Ref. 5]. The system under study is the one where anorthite is the primary phase present. It has a triclinic crystal structure and chemical composition $CaO{\cdot}Al_2O_3{\cdot}2SiO_2$. This

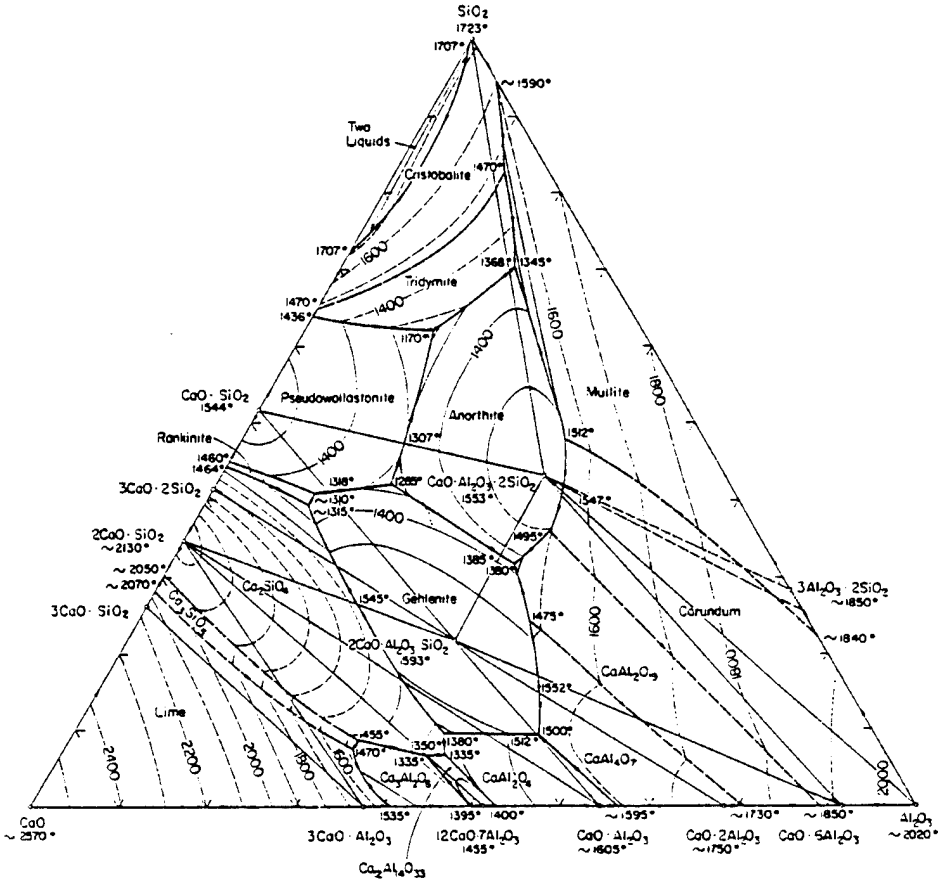

Figure 1. CAS Phase Diagram [Ref. 5]

matrix has also been shown to contain small alumina particles of average size 2μm in amounts below the limits of detection by x-ray diffraction (XRD) (<1.0%). Glassy regions typically account for less than 0.5 volume percent of the matrix. Small amounts of zirconia (ZrO_2) are added to act as a nucleating agent. Due to the low solubility of ZrO_2 particles in the glass melt, they present small heterogeneous nucleation sites and lower glass viscosity which in turn lowers the activation energy for crystallization. [Ref. 6]

B. SILICON CARBIDE (SiC) FIBER-REINFORCED CAS COMPOSITES

Improvement in the toughness of glass-ceramics can be achieved by reinforcing the matrix. Although early work has shown improved work of fracture values for both whisker and unidirectional fiber reinforcement, the strength of the material was compromised due to stress concentrations around fibers caused by the relatively large minimum fiber diameter available. The development of small-diameter ceramic fibers has solved this problem.

Silicon carbide fibers (Nicalon, Nippon Carbon Company: a polymer-melt spun fiber comprising a mixture of fine β-SiC crystals in an amorphous matrix) are used to reinforce the CAS matrix. The properties of the reinforced glass-ceramic and its constituents are shown in Table I.

Material Property	**CAS**	**SiC**	**SiC/CAS**
Nominal composition	$CaO{\cdot}Al_2O_3{\cdot}2SiO_2$	SiC	$CaO{\cdot}Al_2O_3{\cdot}2SiO_2$
Maximum Use Temperature, (°C)	1350	1200	1300-1350
Density, (g/cm^3)	2.76	2.55	2.70
Elastic Modulus, (GPa)	98	193.2	124
Tensile Strength, (MPa)	124	2760	503
Coefficient of Thermal Expansion ($x\ 10^{-6}$ / °C)	5.0	3.1	4.0

Table I. CAS, SiC, and SiC/CAS Material Properties

The reinforcement improves elastic modulus by 27% over that of monolithic CAS and the tensile strength by a very impressive 300%. The improved strength is due to load

sharing between the fiber and matrix. The improvement in toughness is due to energy absorption during fiber pull-out after matrix cracking and fiber/matrix debonding as well as crack blunting and deflection. The dependence of the toughness on the nature and strength of the fiber/matrix interface is illustrated in Figure 2. Region (a) shows fibers that are too weak to improve strength or toughness over all ranges of fiber/matrix bond strength due to no load sharing. Area (b) is a region where either the fiber/matrix interfacial bond is too strong or the fiber is too strongly held by radial compressive stresses. For this condition, strength will be improved but not toughness because fiber pull-out is not possible and failure will occur with cracking of the matrix. Region (c) shows the ideal situation where strength improvement is due to load sharing with the stronger fiber and the optimum fiber/matrix bond strength allows pull-out. [Ref. 11]

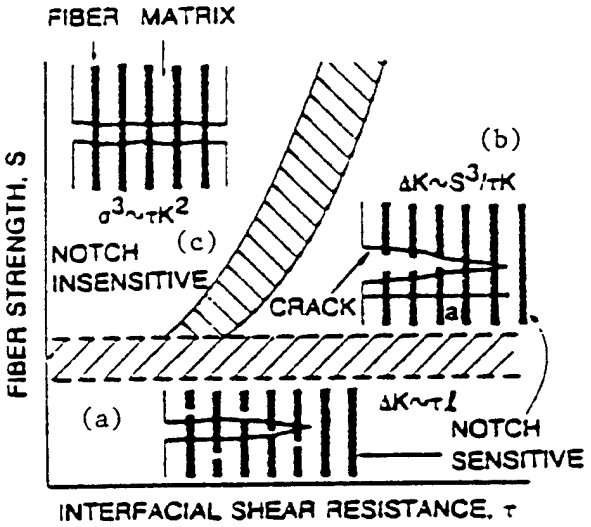

Figure 2. Fracture Mechanism Map for a Uniaxial Fiber Reinforced Ceramic Matrix Composite [Ref. 10]

In the SiC/CAS composite system, the fiber/matrix interface has been shown to consist of two reaction layers; a carbon rich layer next to the fiber and a silicon rich one between the matrix and the carbon layer (normally graphite). These are formed during fabrication by the proposed reaction :

$$SiC_{(s)} + O_{2(g)} \rightarrow SiO_{2(s)} + C_{(s)} \qquad (1)$$

The carbon layer accounts for the realization of the optimal interfacial strength by allowing matrix/fiber debonding to occur [Ref. 13,14]. The interfacial carbon can also act as a diffusion barrier to molecular oxygen. Carbon layer formation can be enhanced by increasing matrix basicity with the addition of small amounts of network modifying oxides, such as As_2O_3. These oxides increase the degree of ionic bonding (or non bridging oxygen) and decrease the silica activity which provides a driving force for the interface forming reaction [Ref. 7,15].

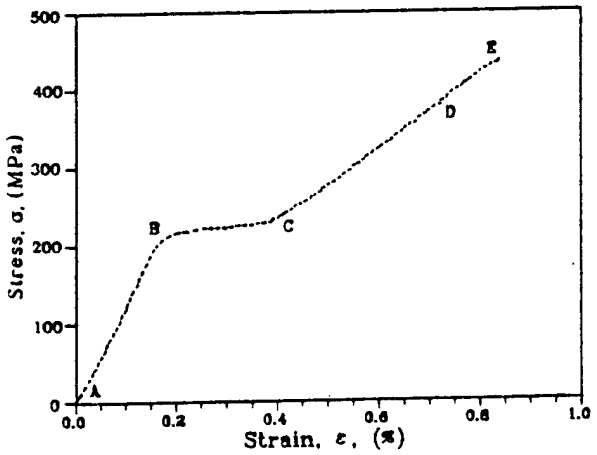

Figure 3. Stress/Strain Curve for $[0°]_8$ SiC/CAS Specimen Under Uniaxial Tensile Loading [Ref. 8]

A typical stress strain curve for $[0^{\circ}]_8$ SiC/CAS (Figure 3) demonstrates the failure mechanisms and process. Region AB corresponds to linear elastic behavior before significant microcracks occur. At point B the matrix begins to crack and fiber/matrix debonding initiates. In region BC transverse crack multiplication occurs until no further matrix failure can occur, at which point the load is carried by the intact fibers alone. This is shown in region CD. Region DE shows final composite failure.

C. CORROSION OF SiC/CAS COMPOSITES BY Na_2SO_4

As noted in the last section, a thin layer of silicon dioxide (SiO_2) forms around the fibers. This film has very low oxygen permeability and acts as an effective barrier to further oxidation of the fiber up to temperatures of about 1500°C. The proposed oxidation process involves six steps: (1) transport of the molecular oxygen through the matrix to the SiO_2 surface, (2) diffusion of oxygen through the oxide film, (3) reaction at the oxide-ceramic interface, (4) transport of product gases through the oxide film, (5) transport of product gases through the matrix and (6) transport of product gases away from the surface. Current research strongly indicates that diffusion of oxygen through the oxide is the rate determining step. As stated previously, it is the low rate of oxygen diffusion through SiO_2 that is responsible for this. The low oxygen permeability of SiO_2 is observed only when it is a solid. Once the oxide melts (melting point of 1200°C) or is liquefied (for example, by reaction with Na_2O) it is no longer effective.

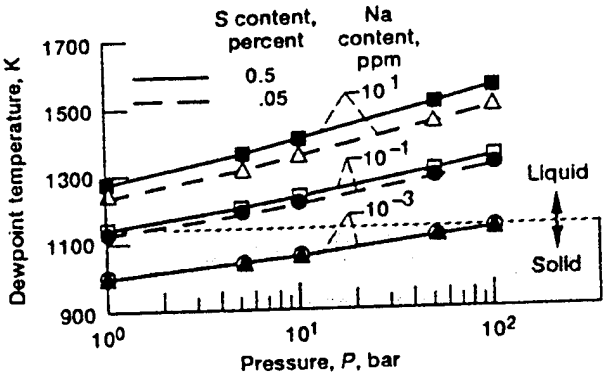

Figure 4. Dewpoints For Na_2SO_4 Deposition [Ref. 4]

In marine environments, deposition of Na_2SO_4 can occur by the following reaction:

$$2NaCl_{(g)} + SO_{2(g)} + 0.5O_{2(g)} + H_2O_{(g)} \rightarrow Na_2SO_{4(l)} + 2HCl_{(g)} \quad (2)$$

Corrosion by Na_2SO_4 is a two step process: deposition on an engine part and actual corrosion. Deposition occurs at the dew point which is a thermodynamic function of temperature and pressure. Corrosion occurs between the dew point and the melting point of Na_2SO_4 (884°C). Figure 4 shows this region for a variety of conditions. Operating at temperatures above the dew point preclude deposition while higher pressures increase deposition due to higher dew points at higher pressures. The regime for hot corrosion is limited, as seen in Figure 5, but since desired engine operating conditions may fall into this area and since the effects of hot corrosion seem to be severe, it is important to understand the processes at work. The proposed reaction scheme for Na_2SO_4 hot corrosion is as follows:

$$Na_2SO_{4(l)} \leftrightarrow Na_2O_{(s)} + SO_{3(g)} \quad (3)$$

$$xSiO_{2(s)} + Na_2O_{(s)} \leftrightarrow Na_2O{\cdot}x(SiO_2)_{(l)} \quad (4)$$

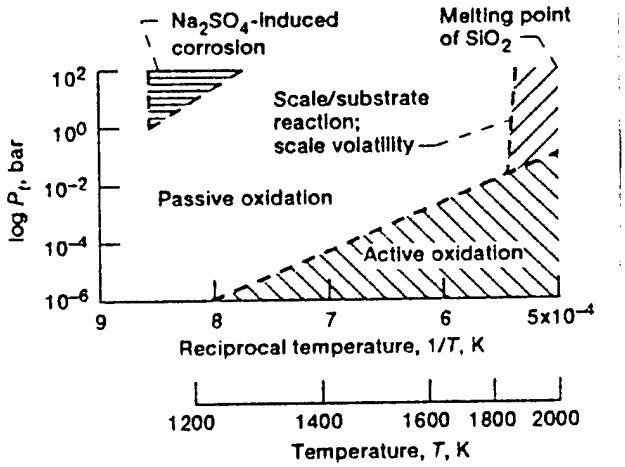

Figure 5. Hot Corrosion Region as a Function of Reciprocal Temperature [Ref. 4]

In general, the corrosion process can be predicted using a simple Lewis acid-base interpretation. SiO_2, an acidic oxide, reacts with Na_2O, a basic oxide, to form a salt, sodium silicate. Reaction (4) is driven by the activity of the molten Na_2O salt. A high activity indicates a basic salt which drives reaction (4) to the right. Low activity Na_2O is termed an acidic salt and the reaction does not proceed since silica does not undergo acidic dissolution. The activity of the Na_2O salt is determined by the partial pressure of $SO_{3(g)}$ (P_{SO3}). Low P_{SO3} increases Na_2O activity while high P_{SO3} decreases it.

Results complied by Jacobson [Ref. 4] indicate that corrosion of SiC can be regulated by control of P_{SO3} which gives credence to use of the acid-base model to predict corrosion but other factors such as secondary elements may make the Na_2O salt basic. For instance, carbon, which drives Na_2O basic, has been shown to increase corrosion rates even with high P_{SO3}. This may also cause problems in the SiC/CAS CMC due to the presence of the carbon interfacial layer. [Ref. 4,16]

The above discussion involved only the corrosion of the fiber. Reactions of the matrix both with the salt and with the fiber corrosion products may also factor into the degradation of material properties of this CMC. Other factors which may accelerate fiber oxidation are the presence of sodium carbonate (Na_2CO_3) or sodium chloride with an excess of water vapor (a condition which exists when an engine is operated in the fuel-rich region). Expected reactions are as follows:

$$Na_2CO_{3(l)} \leftrightarrow Na_2O_{(s)} + CO_{2(g)} \quad (5)$$

$$2NaCl_{(v)} + H_2O_{(v)} \leftrightarrow Na_2O_{(s)} + 2HCl_{(s)} \quad (6)$$

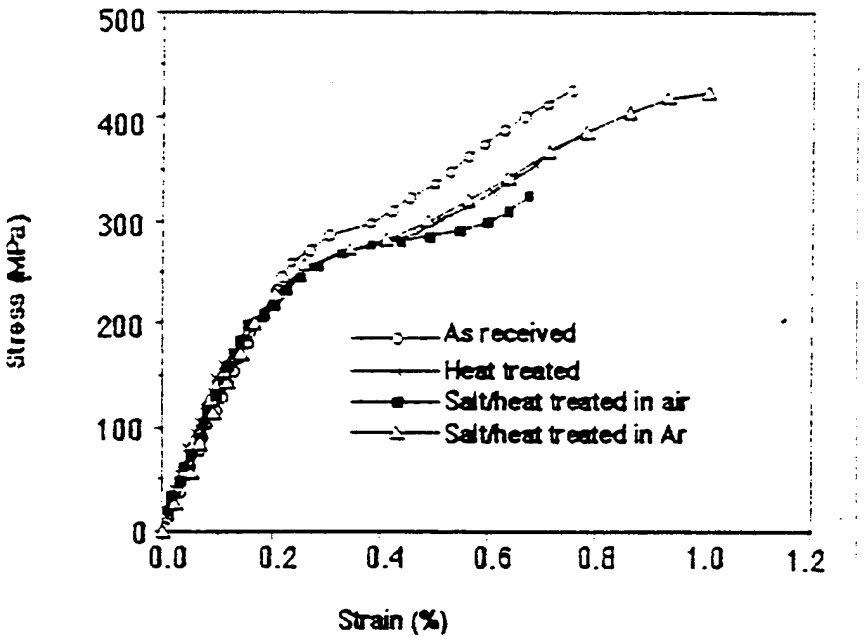

Figure 6. Stress Strain Curves of SiC/CAS Tensile Specimen Exposed to Various Environments [Ref. 17]

Material property degradation due to sodium sulfate corrosion of SiC/CAS CMC has been demonstrated by Wang, Kowalik, and Sands (see Figure 6). They found a reduction in tensile strength of about 25% in SiC/CAS when coated with Na_2SO_4 salt and heat treated in air at 900°C while heat treatment in an argon atmosphere led to less than 10% reduction.

Corrosion studies have also been carried out by Newton [Ref. 18] on uncoated and Na_2SO_4 coated samples both in air and argon atmospheres at 900°C for 100 hours which supported observations of Wang, Kowalik and Sands [Ref. 17] that corrosion of the CMC leads to degradation of material properties. The corrosion process proposed by Wang, Kowalik and Sands is that the protective SiO_2 layer on the fiber is dissolved by the salt forming $Na_2O{\cdot}x(SiO_2)$. This allows rapid diffusion of oxygen into the fiber and causes the SiC at the composite surface to be completely oxidized. The following reacton was suggested by Wang et al as being the mechanism by which the CAS matrix was attacked by sodium sulfate:

$$Na_2SO_{4(l)} + CaAl_2Si_2O_{8(s)} \leftrightarrow 2NaAlSiO_{4(s)} + CaSiO_3 + SO_{2(g)} + O_2 \qquad (7)$$

These results are the starting point of the present study. [Ref. 17,18]

III. SCOPE OF PRESENT WORK

It was shown in the previous sections that glass ceramic composite matrices, due to their nature, present unique oxidation and corrosion properties. Depending on the fiber and matrix involved, their interactions during Na_2SO_4 hot corrosion may lead to rapid oxidation of the fibers which degrades the mechanical properties of the composite so that it is no longer a viable candidate for Naval applications.

The focus of this present work is the assessment of microstructural changes and chemical mechanisms of the degradation observed in a SiC\CAS CMC when coated with Na_2SO_4 and heat treated for 50 hours at 900°C in air and argon environments and to note any differences between these and similar samples studied by Newton which were heat treated for 100 hours. This will give a qualitative feel for the reaction kinetics.

The treated samples were provided by the Naval Air Warfare Center (NAWC), Warminster, PA. They were treated as follows: (1) as-prepared SiC/CAS, (2) salt coated and heat treated in air (3) salt coated and heat treated in argon. The samples were analyzed by optical microscopy, scanning electron microscopy (SEM) and x-ray diffraction (XRD).

IV. EXPERIMENTAL PROCEDURE

The cerammed SiC/CAS composite was fabricated by Corning Incorporated. The manufacturing process is depicted in Figure 7.

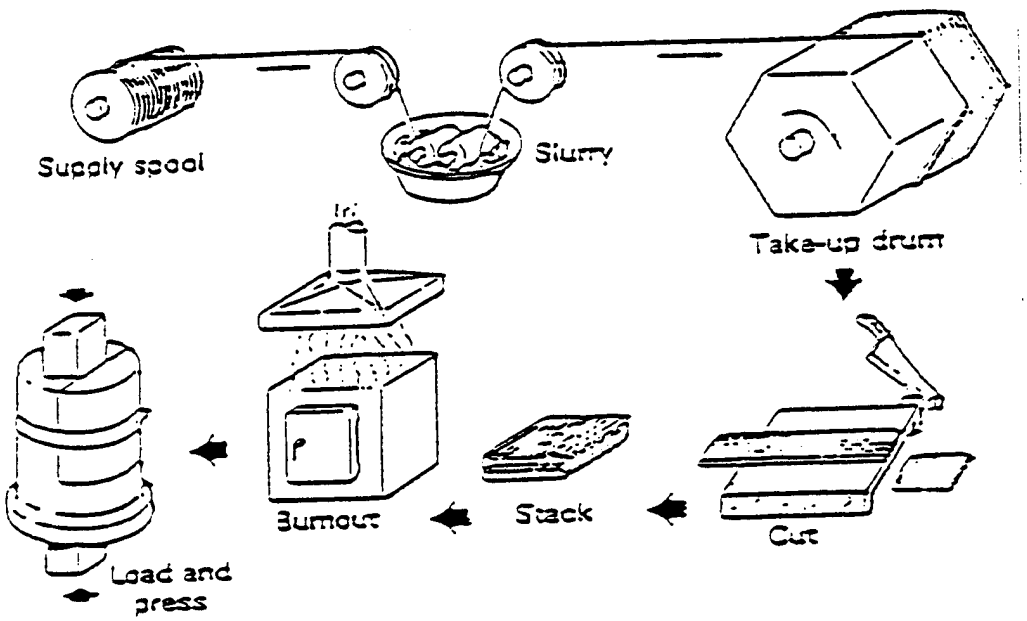

Figure 7. SiC/CAS Fabrication Process Schematic [Ref. 12]

The manufacturing steps were as follows:

1. Impregnation of the uncoated Nicalon SiC fibers with a glass powder slurry. The glass powder was formed from a mixture of SiO_2, CaO, Al_2O_3, As_2O_3 and ZrO_2 (note, As_2O_3 and ZrO_2 were added as nucleating agents) which had been melted together, mixed, quenched in cold water and ground to a powder. The slurry was formed by mixing the powder with a carrier liquid and organic binder.
2. The impregnated fiber was wound onto a take-up drum to form tapes.

3. The tapes were dried, and removed from the drum.
4. Three tapes were stacked in 0° 90° 0° orientation and baked in a furnace at 600°C for 30 minutes to remove the organic binders.
5. The stacks were then hot-pressed under vacuum.
6. They were then partially crystallized (cerammed) at 900° C for 24 hours.

The samples used in this study were then treated by Dr. S. Wang, Aircraft Division, at the Naval Air Warfare Center (NAWC) in Wesminster PA . The samples were received as follows:

1. As-prepared.
2. Salt coated (approximately 3.0 mg/cm^2 of Na_2SO_4), heat treated in flowing air at 900°C for 50 hours.
3. Salt coated (approximately 3.0 mg/cm^2 of Na_2SO_4), heat treated in flowing pure argon at 900° C for 50 hours.

Since it had been previously established that there is little to no effect of heat treatment on non-coated samples they were not included in this study [Ref. 1,2,18]. The as-prepared sample was used as a baseline for the analyses conducted. Its matrix composition is provided in Table 2 [Ref. 3]. The samples coated on one side with salt were used to approximate the expected Na_2SO_4 deposition on gas turbine components after combustion of fuels with 0.05% sulfur impurities when operating at 900° C for 500 hours [Ref. 3].

Oxide Components	Composition (wt. %)
CaO	18.5
Al_2O_3	38.5
SiO_2	39.5
ZrO_2	3.0
As_2O_3	0.5

Table II. Matrix Composition

A. OPTICAL MICROSCOPY

A Carl Zeiss Jena (Model 2000) optical microscope was used to observe and photograph the surface and cross sections of the samples. Cross sectional samples were those prepared for scanning electron microscopy (see below).

B. X-RAY DIFFRACTION (XRD)

X-ray diffraction analysis was performed on the unprepared surfaces of the samples and, in the case of the argon sample, the washed surface using a Phillips XRG 3100 X-ray generator and a PW 1710 Diffractometer Controller linked to a Digital 3100 VAX workstation. The system was set up with a copper target (with $K\alpha_1$ and $K\alpha_2$ wavelengths of 1.54060 and 1.54439 Å) and a bent graphite crystal monochromator. The

operating parameters were set at 30 kV and 35 mA. The raw data was collected over a range from 10 to 80 degrees with a scan rate of 0.001 degrees per second.

The data was analyzed using the Phillips APD 1700 software on the VAX workstation to obtain peak positions (both 2θ and d-spacings), and integrated intensities. The data was then plotted and compared to known crystal data (d-spacings, peak intensites, and 2θ positions) using the Phillips Total Access Data Base to identify the crystalline phases present in the sample. The Miller indices of the phases were verified by comparison with the Hanawalt JCPDS diffraction pattern cards.

C. SCANNING ELECTRON MICROSCOPE (SEM)

Cross sections of the samples were cut to provide a 90°/0°/90° fiber orientation exposure. They were then mounted in Konductomet I, a conductive phenolic compound, using a spring clip to keep the sample oriented. This orientation provided a view of the surface corrosion and the depth of corrosion penetration into the matrix. The mounted samples were ground on a rotating wheel with 500, 800 and 4000 silicon carbide grit paper. They were then polished on a rotating wheel with svelte cloth using 6μ and 1μ diamond paste suspension. Note that over-polishing lead to beveled edges and care had to be taken to avoid this , sometimes at the cost of a perfectly smooth sample.

The unmounted sample surface was also examined both without polishing and after gentle polishing using 6μ and 1μ diamond paste suspension on a rotating wheel with svelte cloth.

In order to avoid charging of the samples when bombarded with electrons, they were coated with a conductive layer using a vacuum evaporator. Both carbon and gold layers were used at a thickness of about 250 - 300 Å.

Imaging and analysis of the samples was performed using both a Cambridge S200 SEM with a Kevex Energy Dispersive X-ray Spectrometer (EDS) fitted with a Si-Li Light element (C) detector and a Topcon SM510 SEM with an Oxford Instruments EDS fitted with a Ge-Li light element (B) detector. Both backscattered and secondary electron images were obtained from areas of interest and both quantitative and qualitative chemical analysis was obtained with the EDS and the X-ray Imaging process.

V. RESULTS AND DISCUSSION

A. XRD ANALYSIS

The as-prepared and heat treated samples were analyzed and compared to determine the initial crystalline phases and the subsequent changes from heat treatment during exposure to sodium sulfate. A summary of the results is shown in Table III.

	As-prepared	In Air	In Argon
Anorthite	X	X	X
Nepheline		X	X
Wollastonite		X	
Pseudowollastonite			X
Albite		X	
Corundum	?		
Cristobalite		?	
CaS			?
β-SiC	?	?	?
ZrO_2	?		

Table III. Summary of XRD Results

The XRD pattern for the as-prepared sample is shown in Figure 8. The major phase identified was anorthite ($CaO{\cdot}Al_2O_3{\cdot}2SiO_2$.). This confirmed the composition that was expected from the information in Table II. Other possible phases identified were zirconia (ZrO_2), corundum (Al_2O_3) and β-Silicon carbide (β-SiC). These phases were verified by XRD pattern analysis and are presented in Figure 9.

The XRD patterns of the as-prepared and heat treated samples are shown for comparison in Figure 10. Although there is much overlap between the main anorthite peak at 2θ equal to 27.8° and the product phases, anorthite is still evident in the heat treated samples but at significantly reduced levels indicating corrosion of the matrix. The reduction in intensity of the SiC peak at 35.8° is evidence of fiber corrosion. The presence of glassy phases is evident since there is an increase in the background in the heat treated samples.

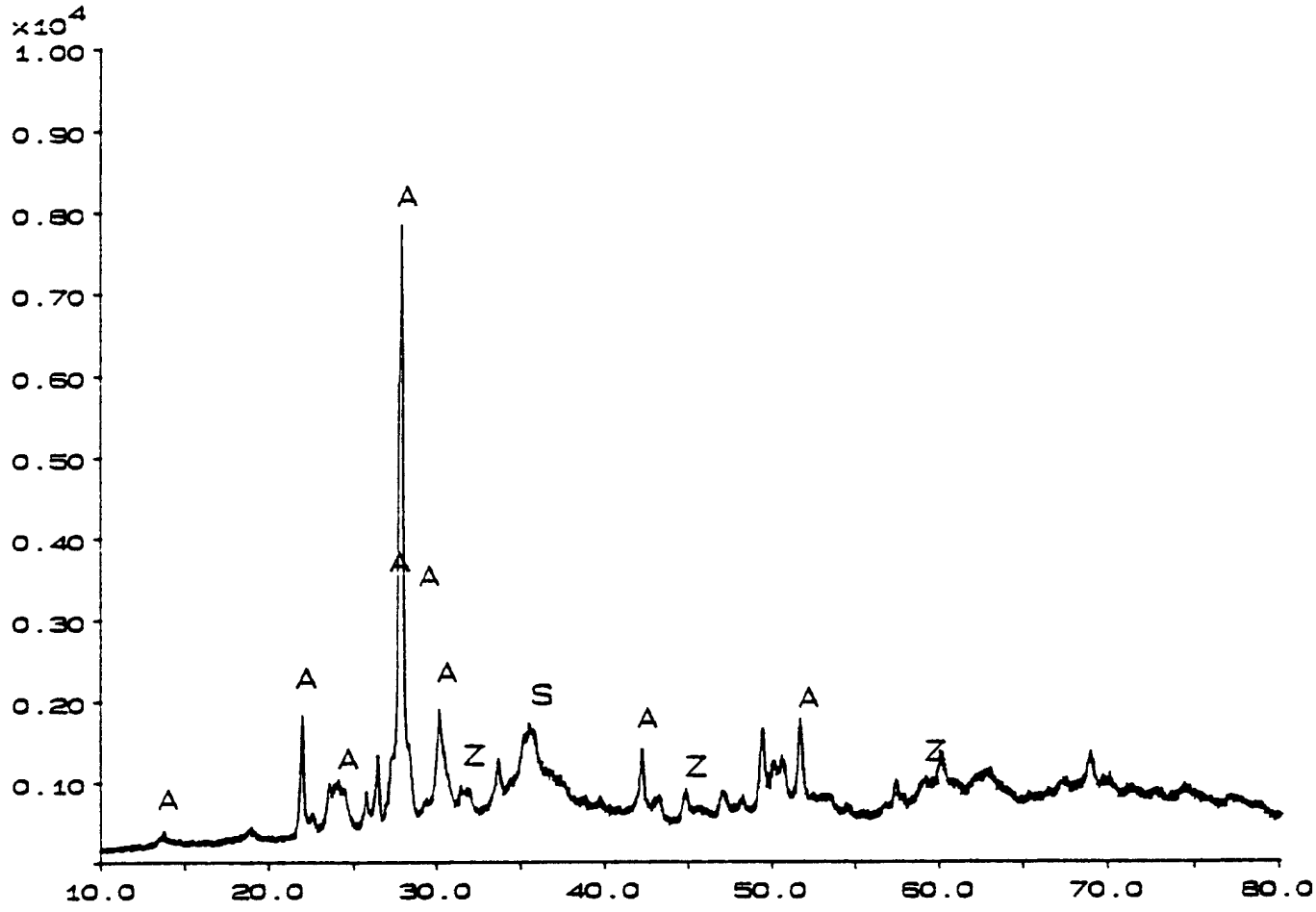

Figure 8. XRD Pattern of As-prepared SiC/CAS Sample
Showing Crystalline Phases A=Anorthite, Z=Zirconia, S=SiC

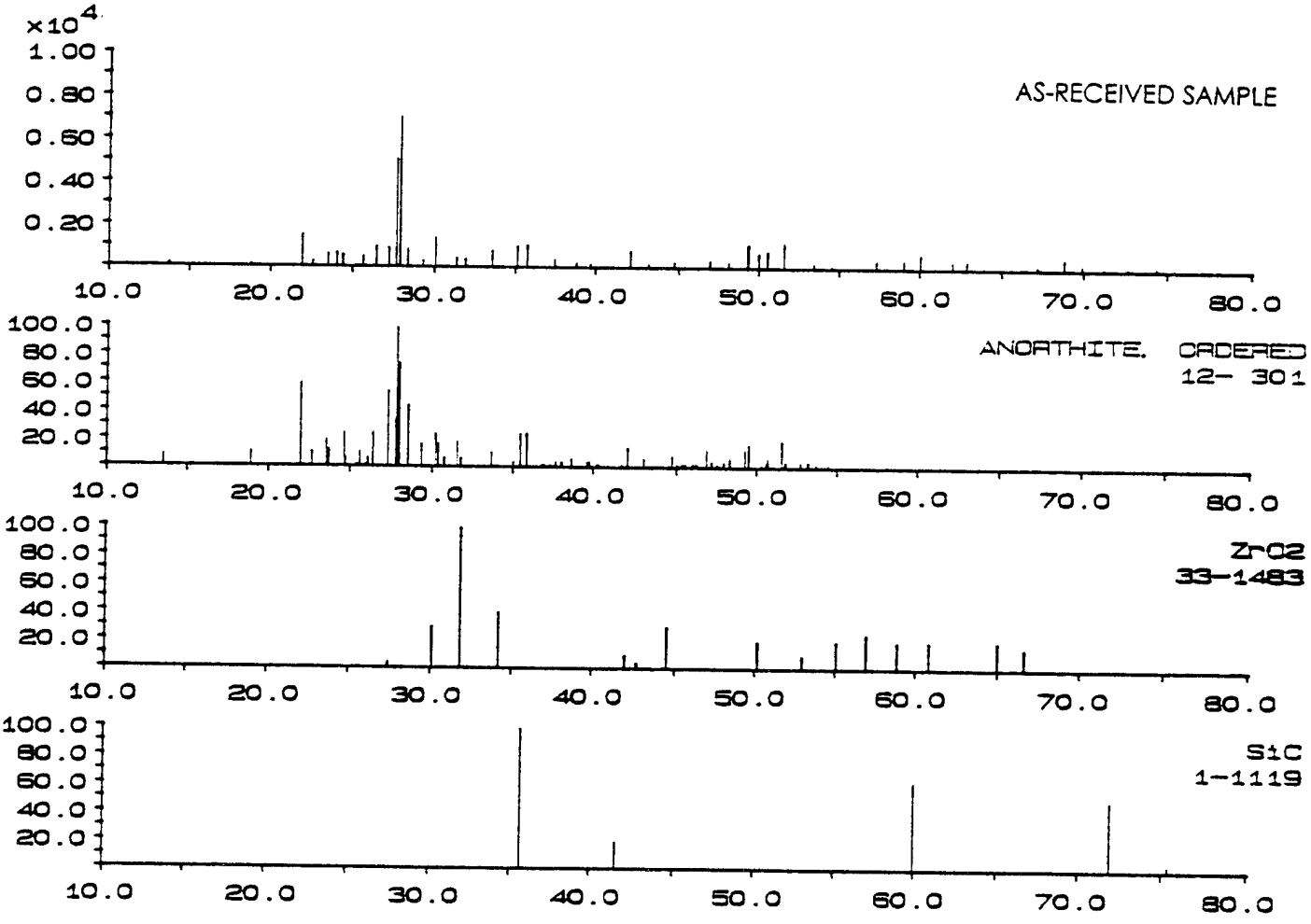

Figure 9. XRD Line Patterns of Phases Present in As-prepared SiC/CAS

(a)

(b)

(c)

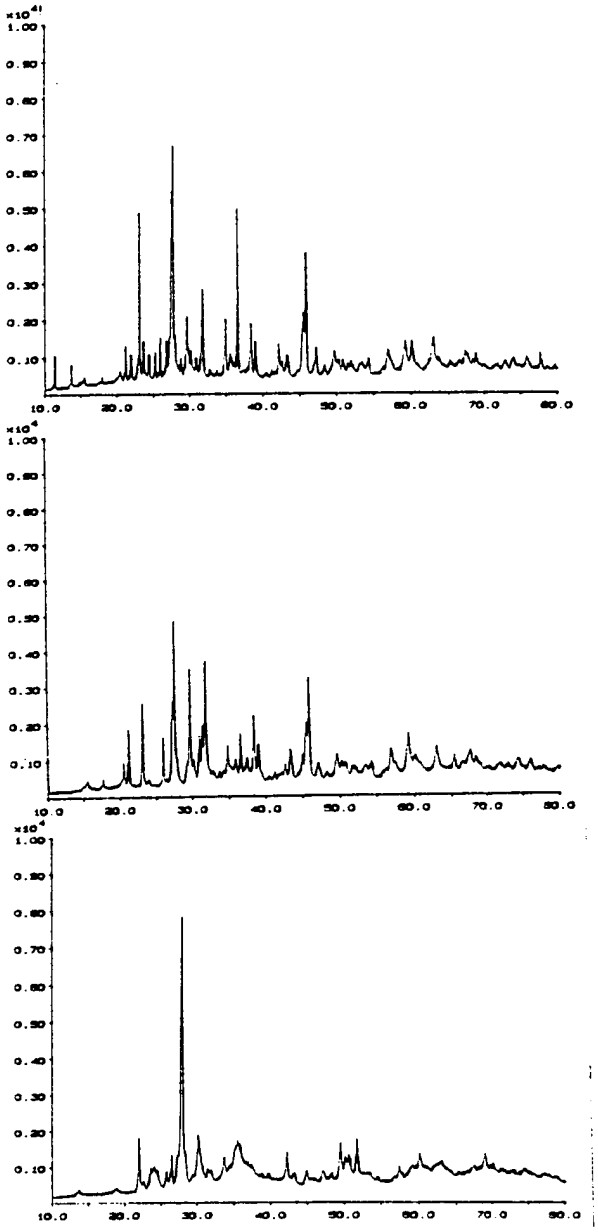

Figure 10. Comparison of XRD Patterns of (a) As-prepared, (b) Salt Coated and heat treated in air and (c) Salt Coated and Heat treated in Argon

XRD analysis results for the salt coated and heat treated in air sample is shown in Figures 11 and 12. New major phases identified were nepheline ($NaAlSiO_4$), wollastonite ($CaSiO_3$) and albite ($NaAlSi_3O_8$). There was also evidence for trace amounts of cristobalite (SiO_2).

The results for the sample salt coated and heat treated in argon are shown in Figures 13 and 14. The new major phases identified are nepheline, pseudowollastonite ($CaSiO_3$) and calcium sulfide (CaS). Identical results were obtained for an argon sample which had been boiled in distilled water for one hour to remove any residual salt in the surface. This was taken as evidence that all or most of the sodium sulfate had undergone reaction.

The formation of pseudowollastonite is interesting because according to the $CaO{\cdot}SiO_2$ equilibrium phase diagram it should not form at temperatures below 1125°C at 1.0 atmosphere (Figure 15).

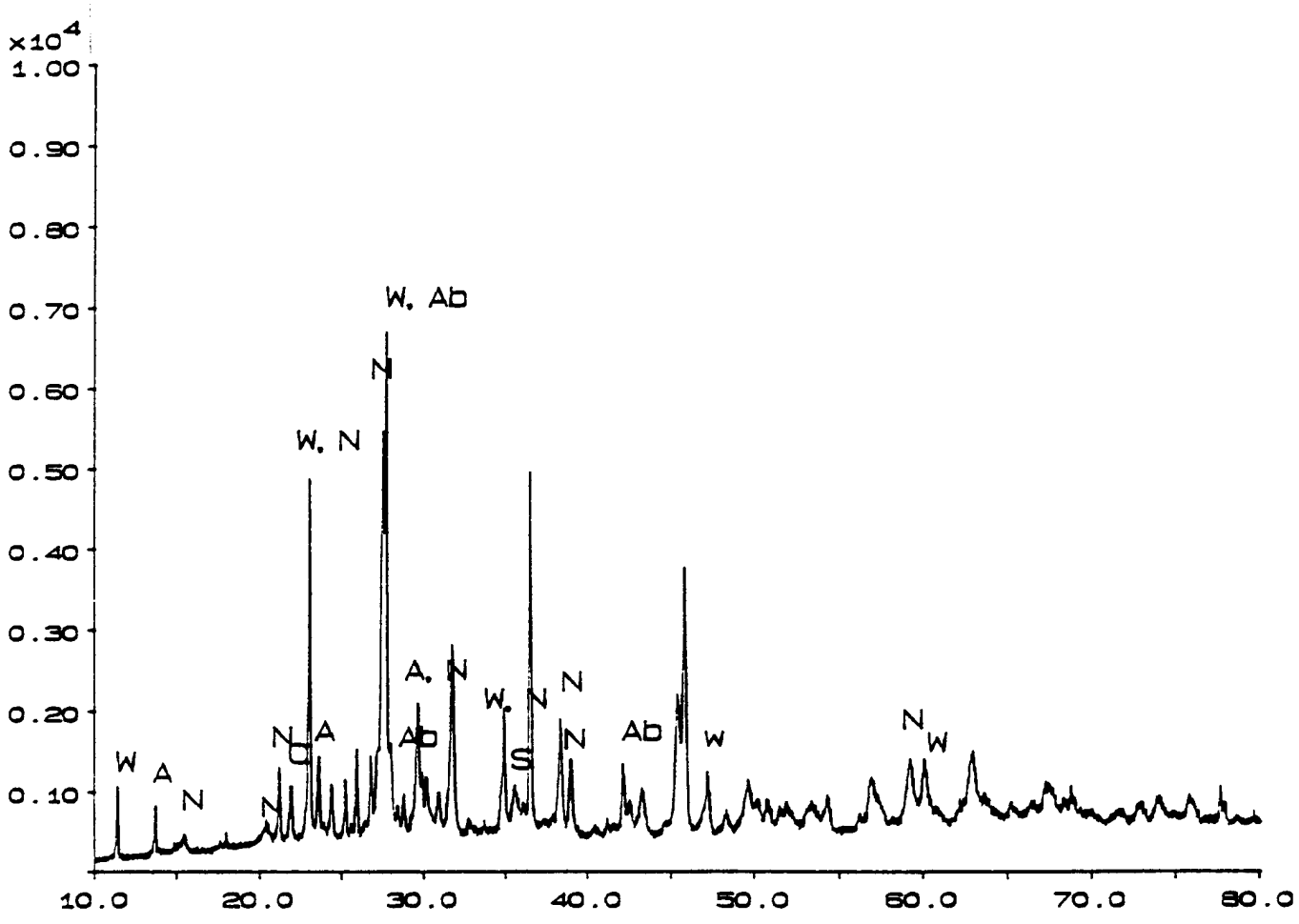

Figure 11. XRD Pattern of SiC/CAS Sample Heat Treated in Air Showing Crystalline Phases A=Anorthite, Nepheline=N, Wollastonite=W, Albite=Ab, Cristobalite=C, S=SiC

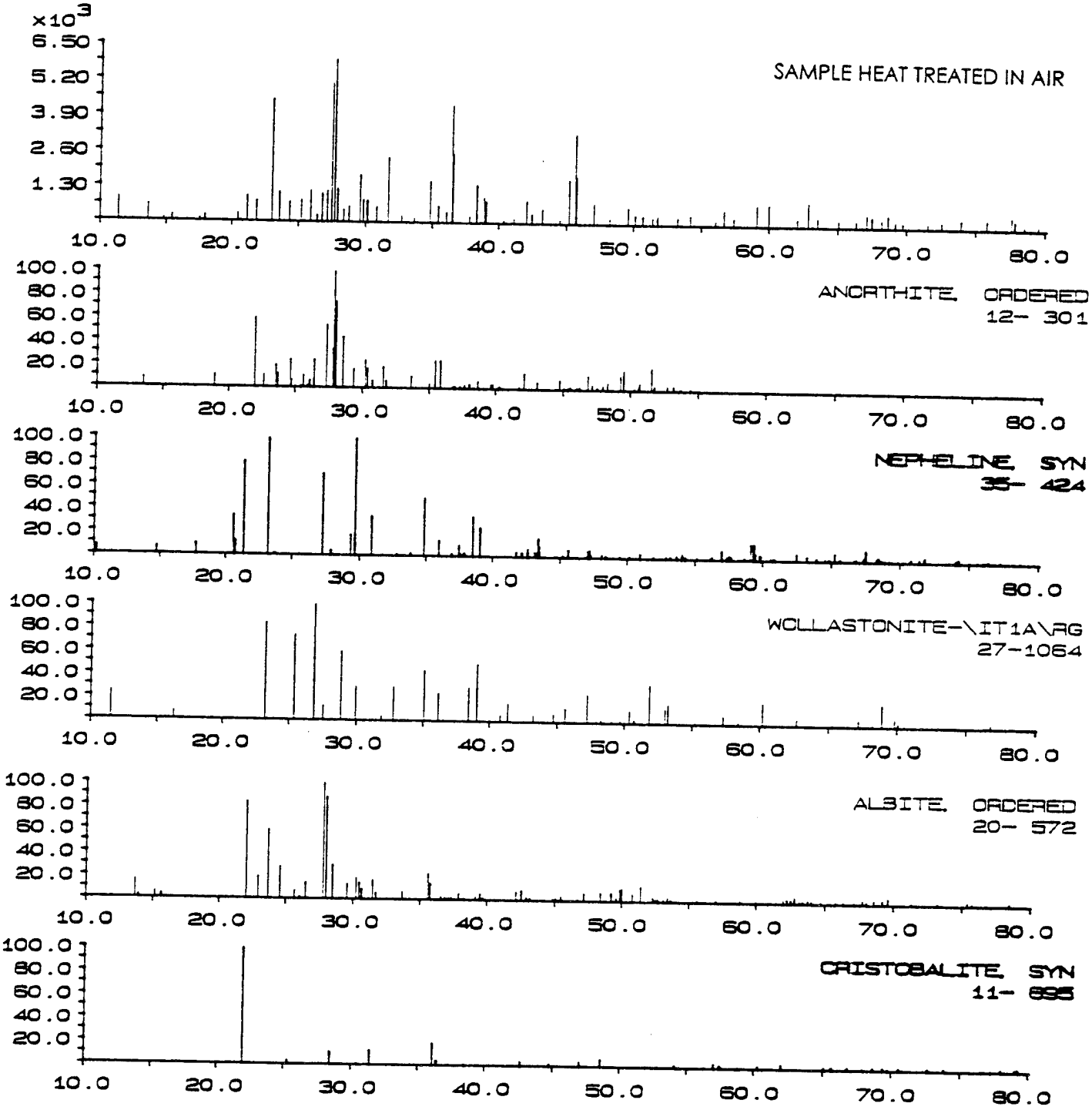

Figure 12. XRD Line Patterns of Phases Present in SiC/CAS Heat Treated in Air

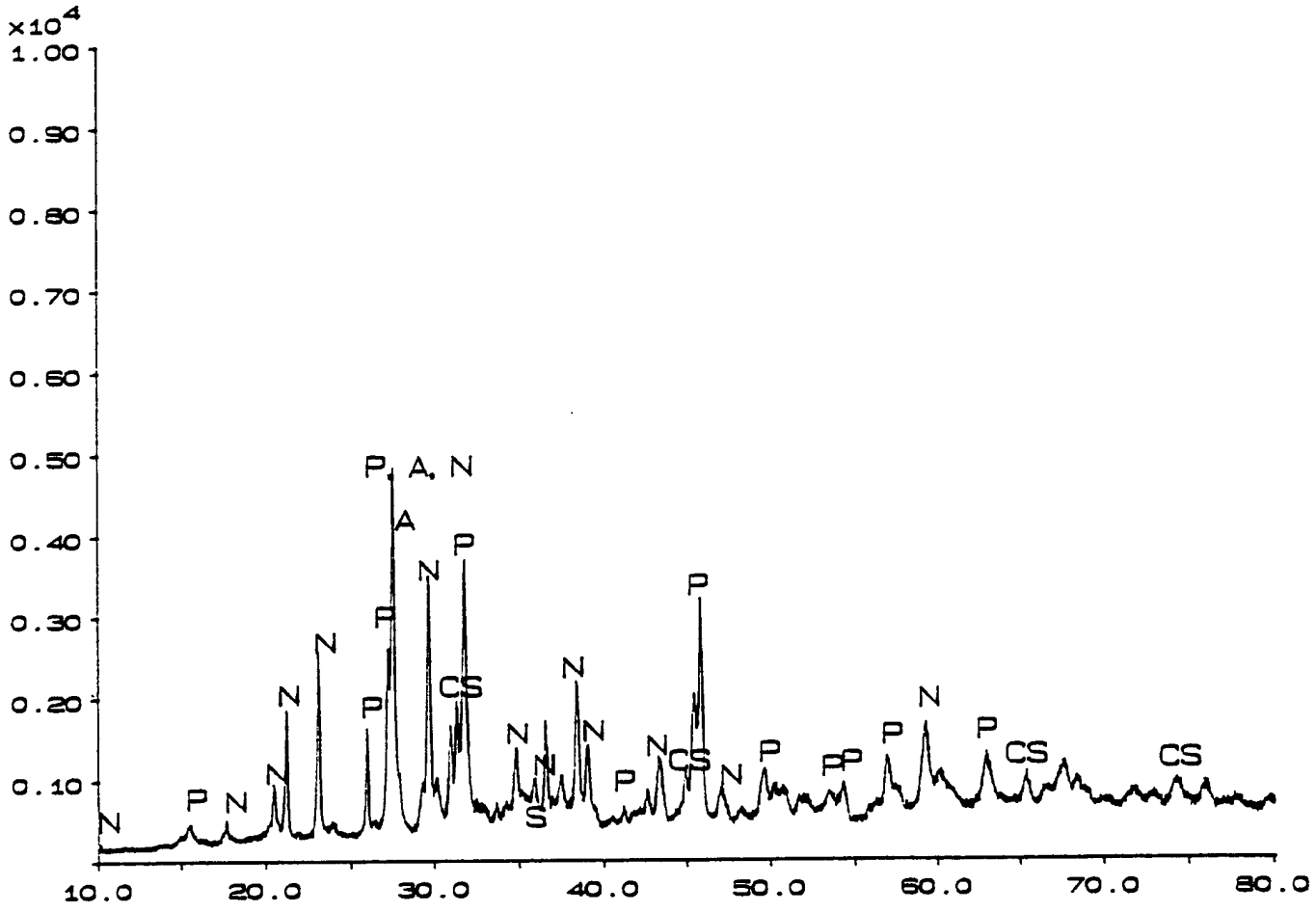

Figure 13. XRD Pattern of SiC/CAS Sample Heat Treated in Argon Showing Crystalline Phases A=Anorthite, Nepheline=N, Pseudowollastonite=P, Calcium sulfide=Cs, S=SiC

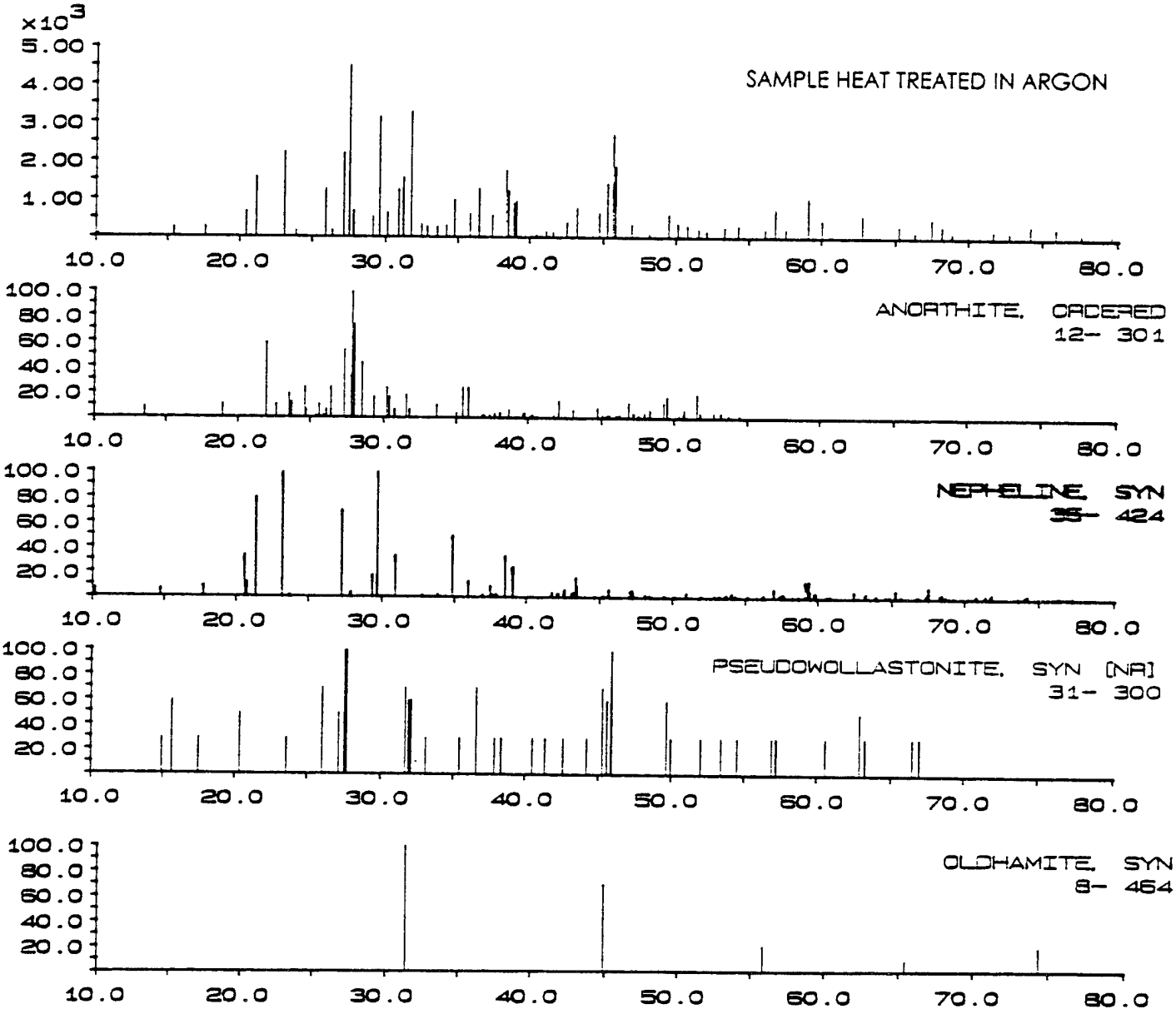

Figure 14. XRD Line Patterns of Phases Present in SiC/CAS Heat Treated in Argon

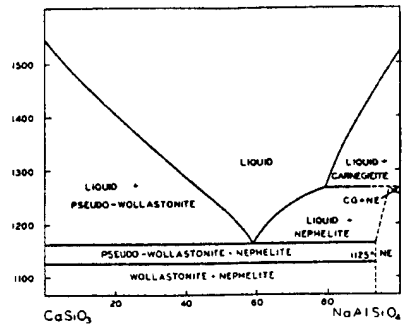

Figure 15. System $CaO{\cdot}SiO_2$-$Na_2O{\cdot}Al_2O_3{\cdot}2SiO_2$ Phase Diagram [Ref. 5]

B. OPTICAL AND SCANNING ELECTRON MICROSCOPY ANALYSIS

An optical micrograph of a cross section of the as-prepared sample showing the [0°] fiber orientation is shown in Figure 16. The sample shows fibers with sized in the range of 12 to 20 μm with fairly uniform distribution in the CAS matrix.

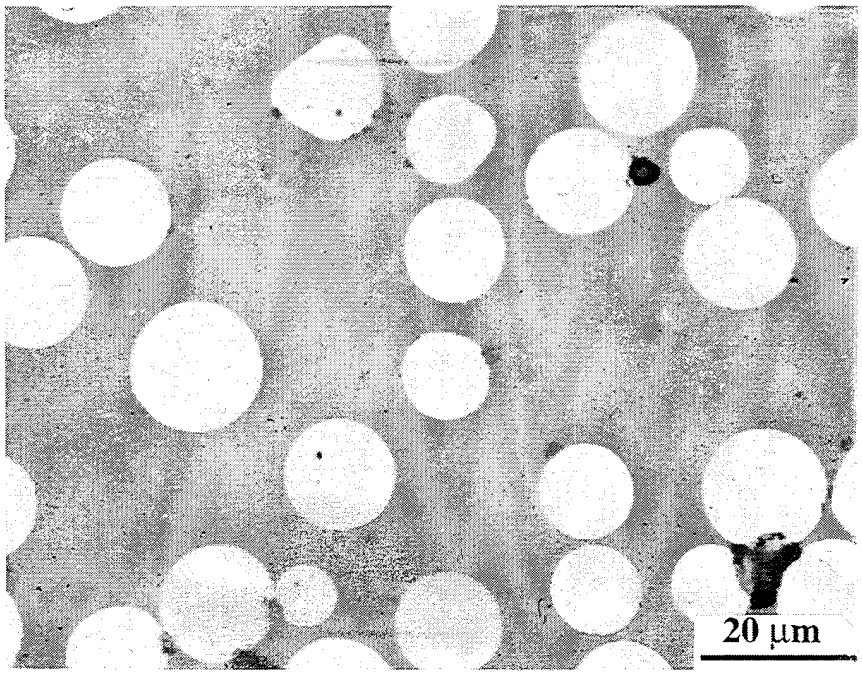

Figure 16. Optical Micrograph of the As-prepared Sample

Faint dark areas were noted around the fibers in the optical micrograph and were assumed to be due to topographical effects but they were still visible in the backscattered electron image (Figure 17). In the backscattered image, (with the detector settings used), it is atomic number differences which are seen rather than topographical effects.

Quantitative EDX analysis results of the matrix are presented in Table III along with the expected composition as provided by NWAC. The significant differences in composition may be attributed to oxide segeregation resulting from non-homogeneous batch processing or formation of glassy areas. This may explain the rings noted above, if calcium or silicon were preferentially depleted in the areas around the fibers, since this would lower the overall atomic number and produce the dark areas. Another possibility is that the analysis, which was quite sensitive to the tilt angle of the specimen, gave inaccurate results. The low As_2O_3 amounts are not alarming since the limit of detection for this analysis is $\pm$ 1 weight percent and the arsenic L x-ray peak overlaps with the aluminum K peak.

Oxide Component	Weight %	Expected Weight % (NWAC)
CaO	20.46	18.5
Al_2O_3	33.82	38.5
SiO_2	42.17	39.5
ZrO_2	3.25	3.0
As_2O_3	0.02	0.5

Table IV. As-prepared SiC/CAS EDX Results and Expected Compositions [Ref. 3]

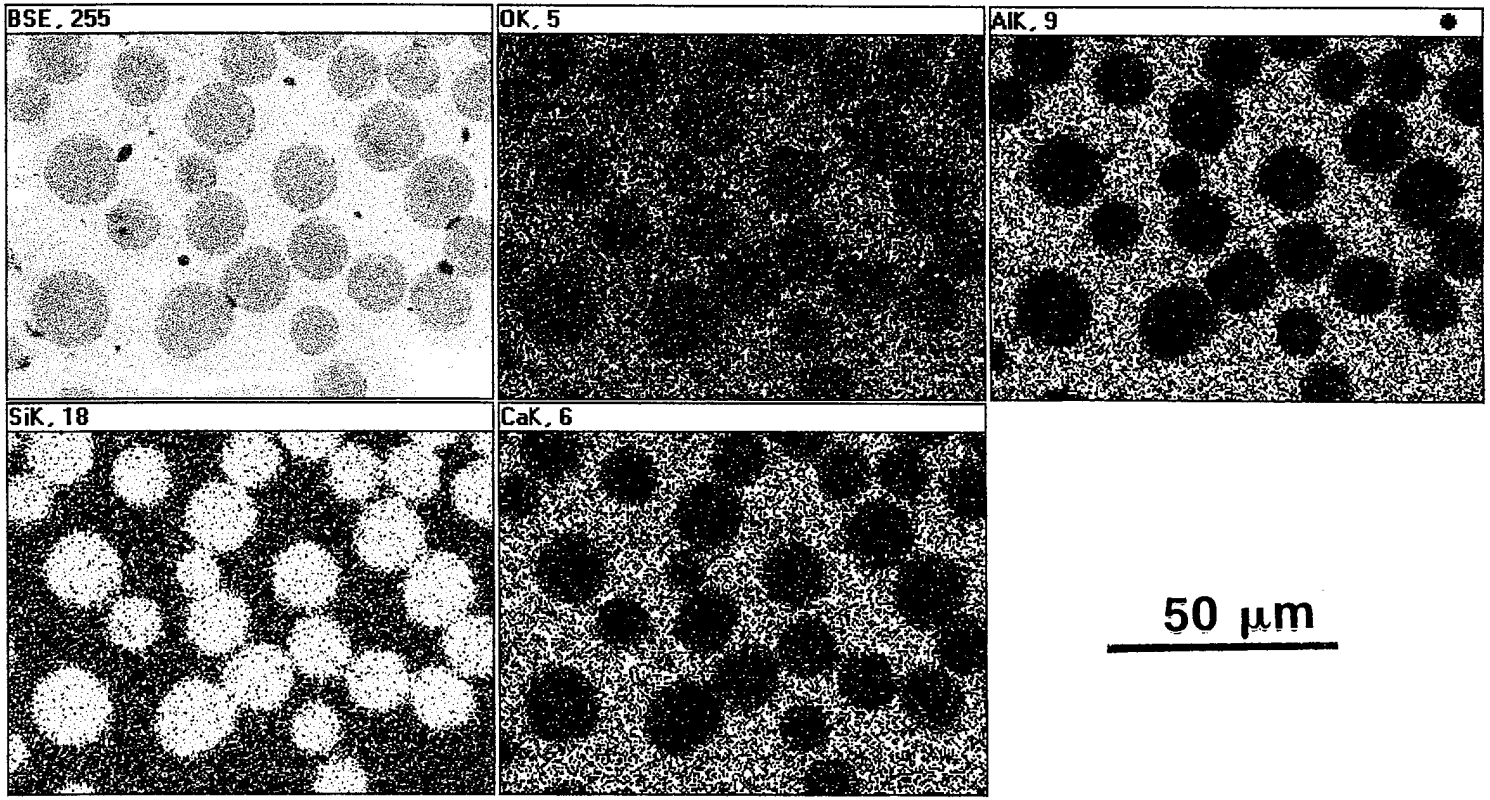

Figure 17. BSE SEM Micrograph and EDX Maps of the As-prepared Sample

The optical micrograph of a sample hot corroded in air is shown in Figure 18. The reaction zone appeared to be about 80 to 100 μm. The surface fibers had been totally corroded and a fine needle like compound was formed in a darker matrix. Just below the surface, partially corroded fibers are evident. Further in from the surface (> 150 μm) the CMC appears unaffected and crack blunting by the fibers could be clearly seen.

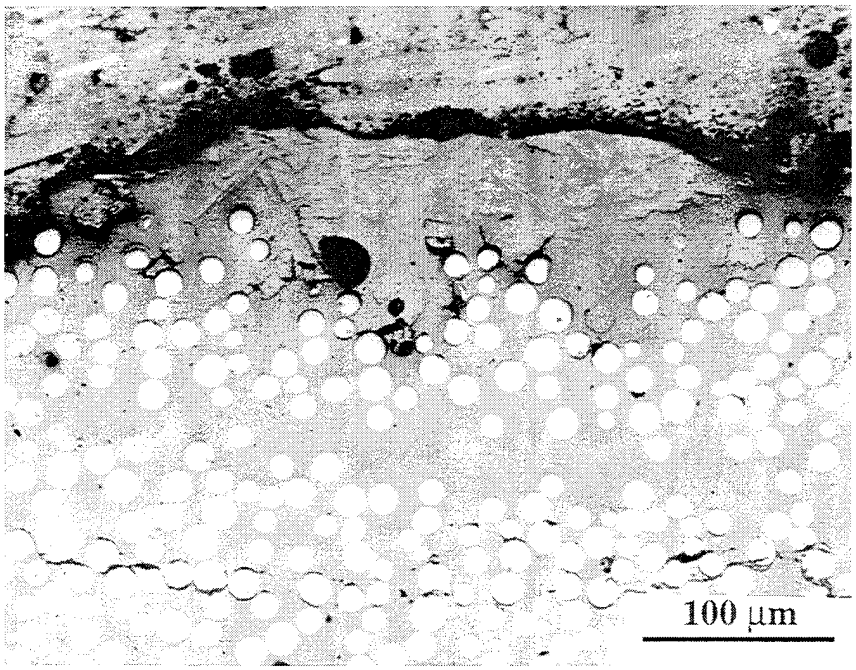

Figure 18. Optical Micrograph of the Sample Heat Treated in Air

The SEM backscatter and EDX element map results for this sample are shown in Figures 19 and 20. Tables V and VI summarize the products expected from the XRD analysis with their elemental weight percents and the analytical EDX results. The 80 -100 μm reaction zone shows significant fiber and matrix attack. This zone also corresponds to the depth of sodium infiltration into the CMC, as is seen on the sodium element map. Near the surface needle like and globular phases have been formed. These have been identified as calcium silicate by EDX analysis and should be wollastonite according to the XRD results. It appears that the finer needle like morphology occurs nearer the surface while the globular morphology is formed further in. Also, the globular form is generally seen within a dark ring area which is suggests that the area is where a fiber had corroded and resulted in a high silica region.

There appear to be two other distinct reacted areas; a darker and a lighter corroded matrix. Elemental analysis of these regions along with the XRD results suggests the presence of albite in the lighter area and nepheline in the darker. The sodium levels quantified are below stoichiometric levels. This may be due to the formation of glassy phases and/or formation of a metastable crystalline phase.

An elemental analysis line map was performed across a partially corroded fiber (Figure 21). The BSE count across the fiber from the reacted matrix to a crack to an outer ring and inner fiber and out again to the unreacted matrix are fairly constant across each region indicating a fairly homogeneous composition. A rise in oxygen and a drop in

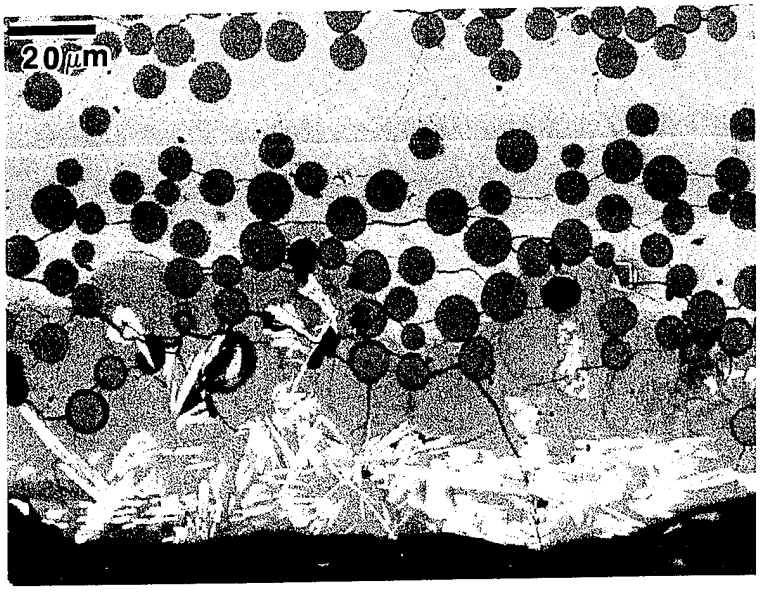

Figure 19. BSE SEM Image of the Sample Heat Treated in Air

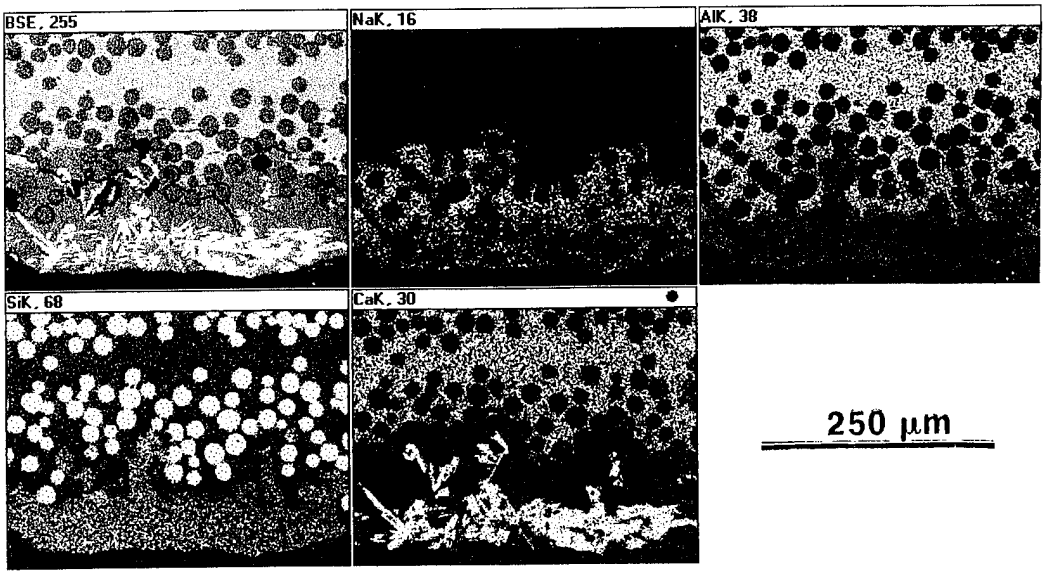

Figure 20. BSE SEM Micrograph and EDX Maps of the Sample Heat Treated in Air

	Na	Al	Si	S	Ca	O
Anorthite $CaAl_2SiO_8$		19.39	20.19		14.41	46.01
Wollastonite / Pseudowollastonite $CaSiO_3$			24.18		34.5	41.32
Nepheline $NaAlSiO_4$	16.18	18.99	19.76			45.05
Albite $NaAlSi_3O_8$	8.77	10.29	32.13			48.81
Oldhamite CaS				44.44	55.56	

Table V. Elemental Weight Percents for Expected Products (deduced from XRD) in Corroded Samples

Area	Na	Al	Si	S	Ca	O	Zr	As
A	0.69	1.48	23.42	0.05	32.86	41.4	0	0.02
B	0.49	0.95	22.82	0.17	34.41	40.88	0	0
C	4.27	9.07	33.78	0.05	2.78	49.39	0	0.72
D	7.17	18.6	22.95	0	1.27	46.8	2.94	0.2
E		18.55	19.02	0	15.23	45.0	1.91	0.09

Table VI. EDX Weight Percent Analysis of Na_2SO_4 Coated Sample Heat treated in Air: A=Needles, B=Globular, C=Dark affected Matrix, D=Lighter affected Matrix, E=Unaffected Matrix

(a)

(b)

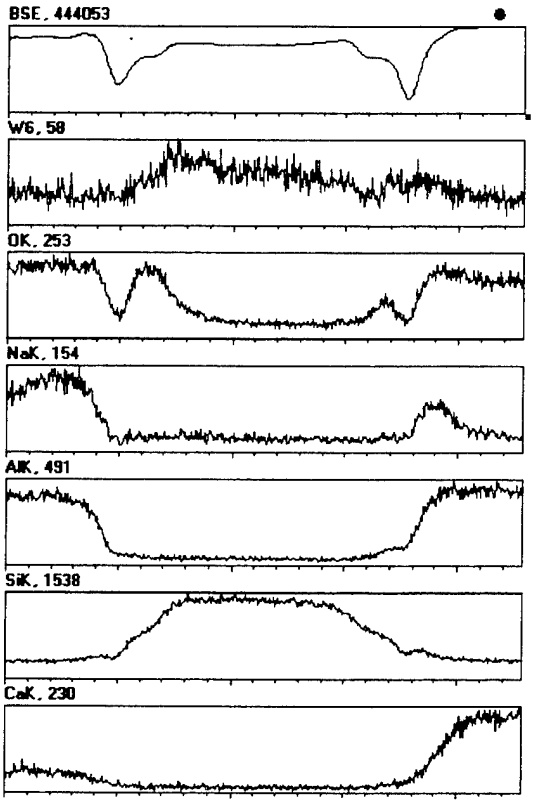

Figure 21. (a) BSE SEM Image and (b) EDX Line Analysis of Partially Corroded Fiber in the Sample Heat Treated in Air

silicon is seen in the outer ring as compared to the inner fiber. This is a clear indication of oxidation of the SiC fiber to SiO_2 The results for sodium are disappointing since point analysis in the ring indicated the presence of sodium in the ring and none in the fiber. This is not obvious from the line scan. Aluminum does show a very slight increase in the ring but lower than expected. These low counts for Na and Al may be due to the high signal to noise ratio and may require a longer signal collection time. The depletion of Ca in the corroded matrix as compared to the uncorroded matrix is also clearly shown.

The optical micrograph of the salt coated sample heat treated in argon is shown in Figure 22. The reaction zone was only about 40 μm which is roughly half the depth of the sample reacted in air. There were globular compounds formed and no evidence of the needle like form was seen.

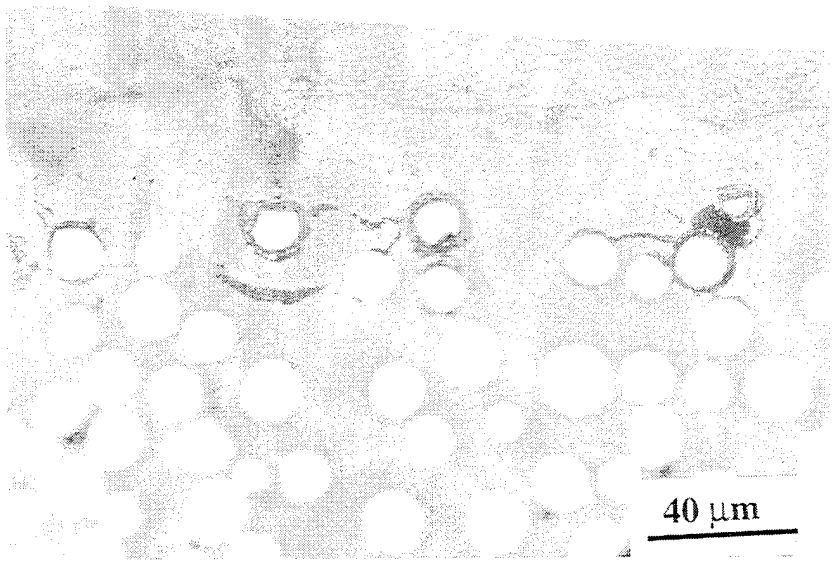

Figure 22. Optical Micrograph of the Sample Heat Treated in Argon

The SEM micrograph and EDX element maps and EDX quantitative analysis of this sample are presented in Figure 23 and Table VII respectivly. It appears that the globular formations are calcium silicate and the XRD analysis indicates that it is pseudowollastonite. As in the sample treated in air, the reacted zone corresponds to the depth of penetration of sodium. The reacted matrix appears to be comprised of a silicon-rich area were aluminum seems to be depleted and a silicon-poor area where aluminum levels remain the same as in the matrix. These areas should contain nepheline and albite respectivly. Again, as in the sample treated in air, the same posibility of the formation of some metastable intermediate and / or glassy phases exists.

The surface of this sample was also studied. Figure 24 is a SEM micrograph of the unpolished surface. Note the rows globular colonies, these were found to be pseudowollastonite. The surface morphology suggests that the pseudowollastonite is formed from the fibers. The area between seems to vary in composition but indicates nepheline formation. When the surface was gently polished (Figure 25), extensive surface cracking was evident. The two dark fibers in the center are uncorroded or only partially corroded as they are still capable of crack deflection. The areas with the small bright areas and porosity appear to be a corroded fiber since they do not affect crack propagation paths. A higher magnification of the corroded fiber area clearly shows cracking through this corroded area. There is also extensive porosity. It is in this area that EDX analysis revaled the presence of calcium sulfide (oldhamite, as detected by XRD). This suggests the porosity was formed by the evolution of either SO_3 or CO gas or both during reaction.

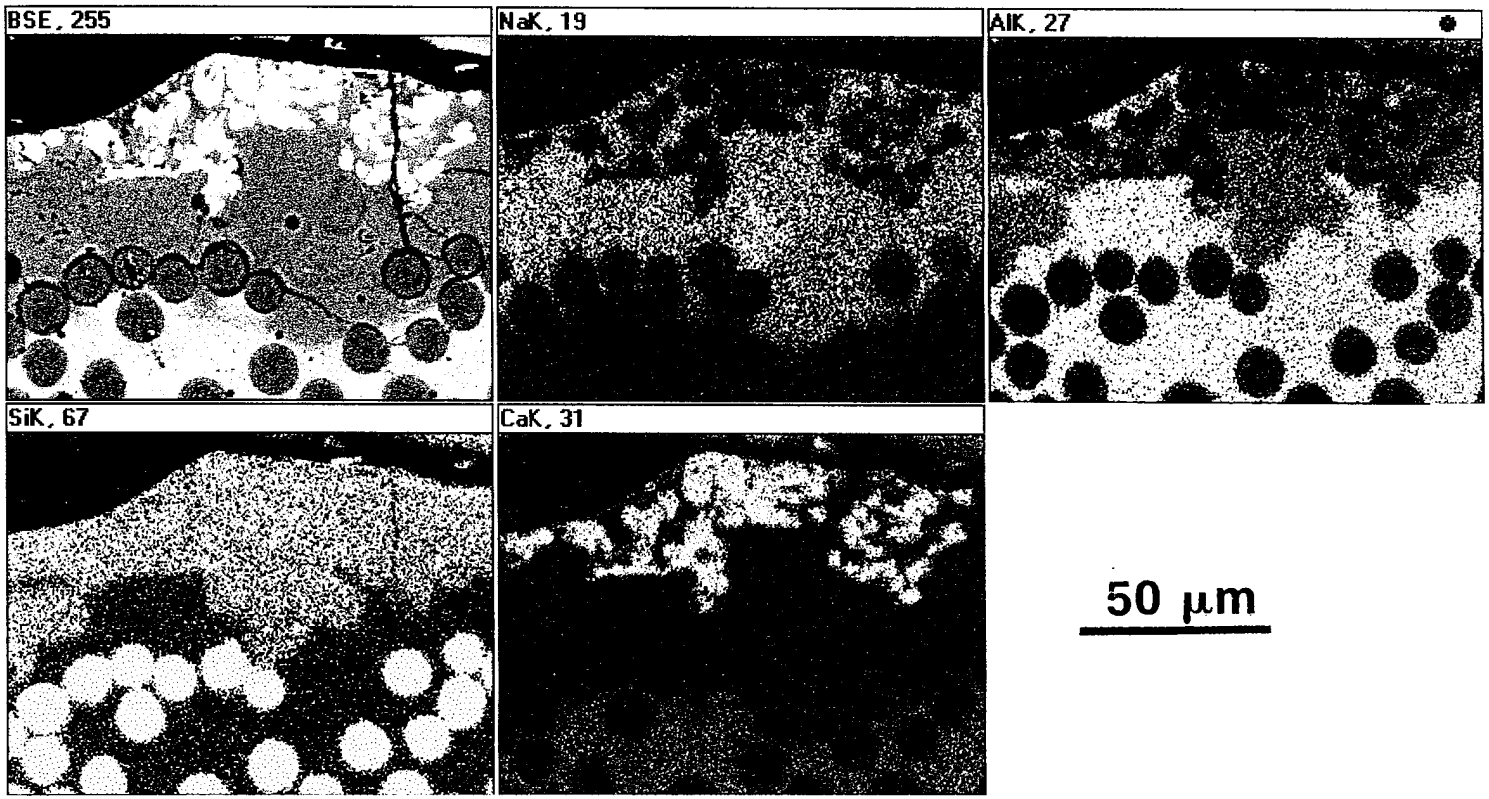

Figure 23. BSE SEM Micrograph and EDX Maps of the Sample Heat Treated in Argon

Area	Na	Al	Si	S	Ca	O	Zr	As
A	0.82	1.13	21.65	0.28	35.38	40.55	0	0.01
B	8.10	18.93	22.11	0	1.57	46.45	2.63	0
C	0.04	17.9	19.71	0.01	14.62	45.13	2.40	0.01

Table VII. EDX Weight Percent Analysis of Na_2SO_4 Coated Sample Heat treated in Argon: A= Globular, B=Corroded Matrix, C= Unaffected Matrix

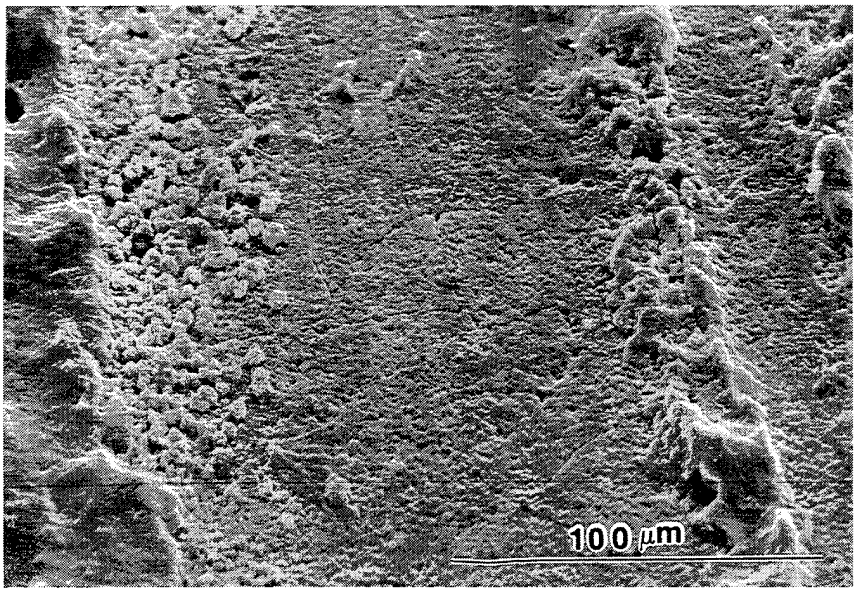

Figure 24. Secondary Electron SEM Micrograph of the Surface of the Sample Heat Treated in Argon - Unpolished

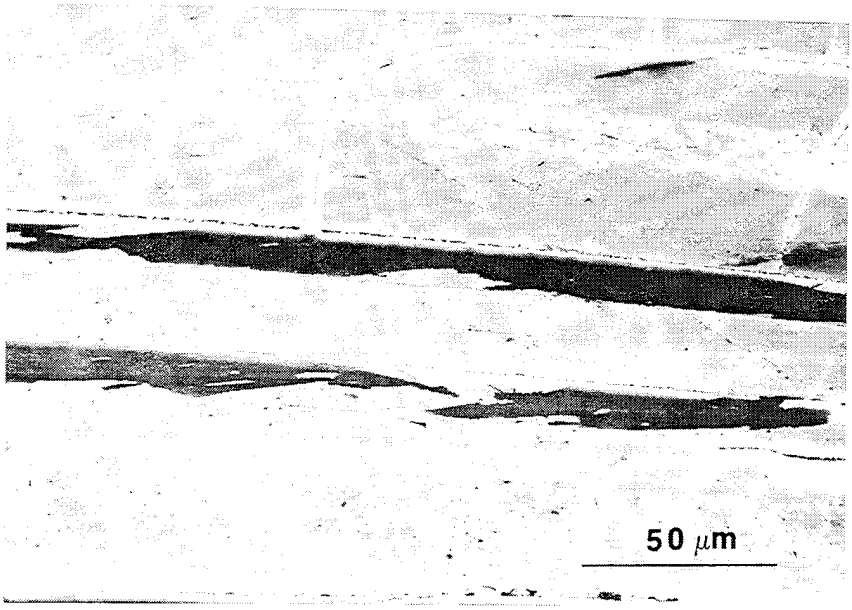

Figure 25. Secondary Electron SEM Micrograph of the Sample Heat Treated in Argon Showing the Polished Surface

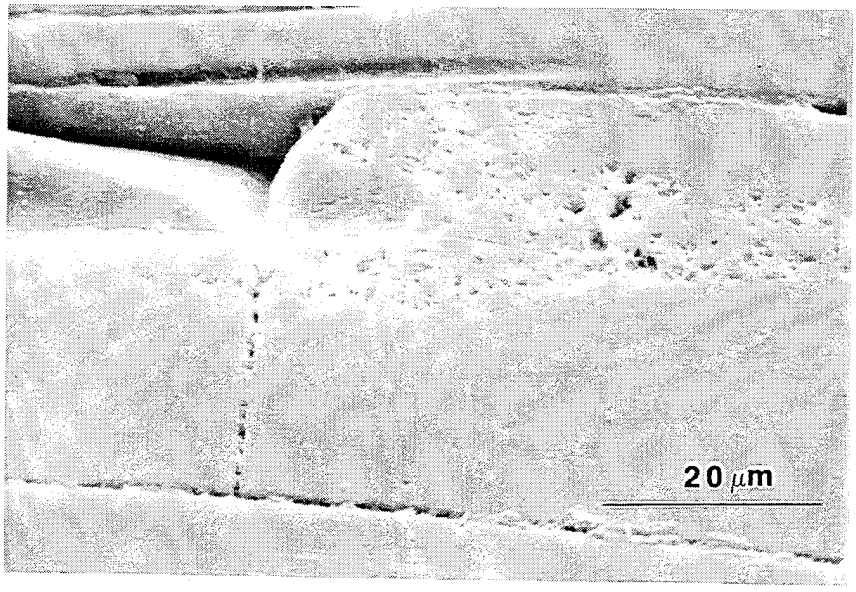

Figure 26. Secondary Electron SEM Micrograph of the Sample Heat Treated in Argon Polished to Show a Corroded Fiber

C. DISCUSSION

The results of this study and the previous work presented in the background section suggest the following reaction mechanisms for the hot corrosion of CAS.

(i) Formation of the sodium oxide from the deposited sodium sulfate:

$$Na_2SO_{4(l)} \leftrightarrow Na_2O_{(l)} + SO_{3(g)} \quad (8)$$

(ii) Attack of the silica layer by the sodium oxide which forms a liquid complex of the two that offers high permeability to oxygen as compared to the solid silica:

$$SiO_{2(s)} + Na_2O_{(l)} \leftrightarrow Na_2O{\cdot}SiO_{2(l)} \quad (9)$$

(iii) Oxidation of the fiber to silica [Ref. 1] which may further react with the sodium oxide:

$$SiC_{(s)} + 1.5\ O_{2(g)} \leftrightarrow SiO_{2(s)} + CO_{(g)} \quad (10)$$

(iv) Attack of the matrix by the salt or the silica complexed with the sodium oxide to form nepheline and calcium silicate. The gases evolved from these reactions could account for the observed porosity in the corroded samples. Ongoing studies on the CAS monolith, at the Naval Postgraduate School by Fox and Kumar, suggest that equation (12) is the slower of the two reactions since hot corrosion of the monolith is not as extensive as in the CAS composite.

$$Na_2O{\cdot}SiO_{2(l)} + CaAl_2Si_2O_{8(s)} \leftrightarrow 2NaAlSiO_{4(s)} + CaSiO_3 \quad (11)$$

$$Na_2SO_{4(l)} + CaAl_2Si_2O_{8(s)} \leftrightarrow 2NaAlSiO_{4(s)} + CaSiO_3 + SO_{3(g)} \quad (12)$$

Albite formation may proceed by the following reaction:

$$Na_2O{\cdot}4SiO_{2(l)} + CaAl_2Si_2O_{8(s)} \leftrightarrow 2NaAlSi_3O_{8(s)} + CaO \quad (13)$$

(v) In the argon environment, oxygen for the corrosion process has been sugested to progress by the following reaction by Kowalik, Wang and Sands [Ref. 2]:

$$Na_2SO_{4(l)} \leftrightarrow Na_2O_{(l)} + SO_{2(g)} + 1/2\ O_{2(g)} \qquad (14)$$

Subsequent reaction product formation may proceed as in the environment with oxygen although a much slower rate is expected. This is supported by the less extensive corrrosion in the argon sample.

It is not known why the morphologies of the calcium silicate are different for the two heat treated samples. At 900°C wollastonite always expected since, according to the equilibrium phase diagram, at one atmosphere pressure pseudowollastonite is only stable above 1125°C [Ref. 5]. It is possible of course that the $CaSiO_3$ is oxygen deficient in the sample annealed in argon so that its true formula is $CaSiO_{3-\delta}$ and it is this oxygen deficiency that leads to pseudowollastonite formation. Further work is needed to substantiate this assertion.

Comparison of results obtained by Newton on similarly coated samples heat treated at 900°C for 100 hours in both air and argon [Ref. 18] reveal some similarities and differences. Both studies found that nepheline, albite and calcium silicate (as wollastonite in the sample heat treated in air and as pseudowollastonite in the sample treated in argon) formed as the major corrosion products. In addition Newton observed formation of a needle like product, identified as rankinite ($Ca_3Si_2O_7$), in both air and argon treated samples. The following reaction was proposed for its formation:

$$3\ CaO + 2\ SiO_2 \leftrightarrow Ca_3Si_2O_7 \qquad (15)$$

This reaction may be a consequence of the longer anealing times during which the local concentration of Na_2O decreases due to its diffusion into the sample and fixed amount. This may affect the activity of the CaO, driving the reaction to the right.

Another product which was identified by Newton in the sample heat treated in argon was mullite ($Al_6Si_2O_{13}$). Its formation was postulated to be due to the oxygen deficient atmosphere. Its formation may be due to the longer heat treatment or it may be a minor product which was not detected.

The formation of cristobalite in the air annealed sample and calcium sulfide in the argon annealed sample were observed in this study and were not found by Newton. Again, these may be minor products which may not always be detected.

VI. CONCLUSIONS

The Na_2SO_4-induced corrosion of SiC fiber-reinforced CAS Glass-ceramic matrix has been studied. The results are summarized as follows:

- Hot corrosion of SiC/CAS at 900°C is significant in an oxidizing (air) atmosphere.
- Hot corrosion of SiC/CAS at 900°C is less severe when exposed in a non-oxidizing (argon) environment.
- Major corrosion products in both environments are nepheline ($NaAlSiO_4$) and calcium silicate ($CaSiO_3$).
- In air, the $CaSiO_3$ has the wollastonite structure. The two morphologies observed, a fine needle like form and a globular form, may be caused by different rates of formation. There are also indications that albite ($NaAlSi_3O_8$) and cristobalite (SiO_2) are formed.
- In argon, the $CaSiO_3$ has the pseudowollastonite structure, a high temperature form of calcium silicate. There is also evidence for the formation of calcium sulfide (CaS).
- We find good correlation between our results and the properties and proposed mechanisms reported by Wang, Kowalik and Sands [Ref. 1]. The degradation of material properties corresponds to the extent of corrosion. The sample exposed to the air environment experienced greater corrosion and showed the most degradation of material properties (see Figure 6).

VII. RECOMMENDATIONS

There are further questions about this CMC which may be addressed by Transmission Electron Microscopy (TEM). Formation of pseudowollastonite may be verified by diffraction studies in the TEM. If its presence is confirmed then the question still remains to be answered as to how it is formed.

TEM may also be used to investigate the interface between the fiber and matrix in the corroded and uncorroded samples. This interface has been proven crucial in determining the properties of the CMC and the effects of corrosion on the interfaces may be critical for maintaining desired material properties.

Protective barrier coatings on the fibers and /or the composite surface may retard oxidation and should be investigated. Consideration of barrier coatings on fibers would again involve investigation of the fiber/ matrix interface to ensure that the desired properties are not degraded.

The kinetics of the corrosion process should be investigated to determine the expected life of engine components. This would provide the basic information necessary to begin a trade-off cost analysis to ascertain if the use of this CMC as a replacement for existing components is warranted.

LIST OF REFERENCES

1. S.W. Wang, R.W. Kowalik, and R. Sands. "Strength of Nicalon Fiber Reinforced Glass-Ceramic Matrix Composites After Corrosion With Na_2SO_4 Deposits", Ceramic Engineering and Science Proceedings, Vol. 13, p. 760, 1992.

2. R.W. Kowalik , S.W. Wang and R.R. Sands, "Hot Corrosion of Nicalon Fiber Reinforced Glass-Ceramic Matrix Composites: Microstructural Effects", Naval Air Warfare Center Technical Report, Warminster, PA, 1992.

3. S.W. Wang, Private Conversation, 1995.

4. N.S. Jacobson, "Corrosion of Silicon-Based Ceramics in Combustion Environments", Journal of American Ceramic Society. Vol. 76, p. 3, 1993.

5. E.M. Levin, C.D. Robbins and H.F. McMurdie, "Phase Diagrams For Ceramics", Vol. I, 1964

6. S.M. Bleay, V.D. Scott, B. Harris, R.G. Cooke. F.A. Habib, "Interface Characterization and Fracture of Calcium Aluminosilicate Glass-Ceramic Reinforced With Nicalon Fibres", Journal of Materials Science, Vol. 27, p. 2811, 1992

7. R.F. Cooper, K. Chyung, "Structure and Chemistry of Fiber-Matrix Interfaces in Silicon Carbide Fiber-reinforced Glass-Ceramic Composites: An Electron Microscopy Study", Journal of Materials Science, Vol. 22, p. 3148, 1992.

8. I.M. Daniel, G. Anastassopoulos and J.-W. Lee. "The Behavior of Ceramic Matrix Fiber Composites Under Logitudinal Loading", Composites Science and Technology, Vol. 46, p. 105, 1993.

9. S.W. Wang, A. Parvizi-Majidi, " Experimental Characterization of the Tensile Behaviour of Nicalon Fibre-Reinforced Calcium Aluminosilicate Composites", Journal of Materials Science, Vol. 27, p. 5483, 1992.

10. K.M. Prewo. "Glass and Ceramic Matrix Composites Present and Future", Material Resources Society Symposium Proceedings, Vol. 120, p. 145, 1988.

11. J. Hsu and R.F. Speyer, "Fabrication and Properties of Sic Fibre-reinforced $Li_2O{\cdot}Al_2O_3{\cdot}6Si_2O_2$ Glass Ceramic Composites", Journal of Materials Science, Vol. 27, p. 381, 1992.

12. K.S. Siskind, "Glass-Ceramic Matrix Composites for Advanced Gas Turbine", AIAA/SAE/ASME/ASEE 26th Joint Propulsion Conference in Orlando FL, 16-18 July, 1990.

13. L.A. Bonney and R. F. Cooper, "Reaction Layer Interfaces in SiC-Fiber-Reinforced Glass Ceramics: A High-Resolution Scanning Transmission Electron Microscopy Analysis", Journal of American Ceramics Society, Vol. 73, p. 2916, 1990.

14. K.M. Knowles, A. Kumar and D.-W. Shin, "Electron Microscopy and Analysis of Fibre-Reinforced Glasses and Glass-Ceramics", Inst. Phys. Conf. Ser No. 119: Section 7, p. 261, 1991.

15. M.H. Lewis and V.S.R. Murthy, "Microstructural Characterization of Interfaces in Fibre-Reinforced Ceramics", Composits Science and Technology, Vol. 42, p. 221, 1991.

16. N.S. Jacobson, J.L. Smialek and D.S. Fox, "Molton Salt Corrosion of SiC and Si_3N_4", Handbook of Ceramics and Composites, Vol. 1, p. 99, 1990.

17. S.-W. Wang, R.W. Kowalik and R. Sands, "Hot Corrosion of Two Fiber Reinforced Glass-Ceramic Matrix Composites", Ceramic Engineering and Science Proceedings, Vol. 14, p. 385, 1993.

18. P. J. Newton, "Sodium Sulfate Corrosion of Silicon Carbide Fiber-Reinforced Calcium Aluminosilicate Glass Ceramic Matrix Composites", Naval Postgraduate School Masters Thesis, 1994.

INITIAL DISTRIBUTION LIST

1. Defense Technical Information Center 2
   Cameron Station
   Alexandria, Virginia 22304-6145

2. Library, Code 52 2
   Naval Postgraduate School
   Monterey, California 93943-5002

3. Professor M.D. Kelleher, Code ME/Kk 1
   Chairman
   Department of Mechanical Engineering
   Naval Postgraduate School
   Monterey, California 93940-5002

4. Professor Alan G. Fox, Code ME/Fx 2
   Mechanical Engineering Department
   Naval Postgraduate School
   Monterey, California 93940-5002

5. Doctor Atul Kumar, Code ME/Ku 2
   Mechanical Engineering Department
   Naval Postgraduate School
   Monterey, California 93940-5002

6. Curricular Officer, Code 34 1
   Department of Naval Engineering
   Naval Postgraduate School
   Monterey, California 93940-5002

7. LT Maria A. Oppici 2
   503 Macintosh Drive
   Mullica Hill, New Jersey 08062

8. Dr. Shaio-WenWang 1
   Code 6063
   Aircraft Division
   Naval Air Warfare Center
   Warminster, Pennsylvania 18974